X-Ray Observations of a [C II]-bright, $z = 6.59$ Quasar/Companion System

Thomas Connor[1,2] , Eduardo Bañados[2,3] , Chiara Mazzucchelli[4] , Daniel Stern[1] , Roberto Decarli[5] , Xiaohui Fan[6] ,
Emanuele Paolo Farina[7] , Elisabeta Lusso[8,9] , Marcel Neeleman[3] , and Fabian Walter[3]

[1] Jet Propulsion Laboratory, California Institute of Technology, 4800 Oak Grove Drive, Pasadena, CA 91109, USA; thomas.p.connor@jpl.nasa.gov
[2] The Observatories of the Carnegie Institution for Science, 813 Santa Barbara Street, Pasadena, CA 91101, USA
[3] Max Planck Institute for Astronomy, Königstuhl 17, D-69117 Heidelberg, Germany
[4] European Southern Observatory, Alonso de Cordova 3107, Vitacura, Region Metropolitana, Chile
[5] INAF—Osservatorio di Astrofisica e Scienza dello Spazio, via Gobetti 93/3, I-40129 Bologna, Italy
[6] Steward Observatory, University of Arizona, 933 N Cherry Avenue, Tucson, AZ, USA
[7] Max Planck Institut für Astrophysik, Karl–Schwarzschild–Straße 1, D-85748 Garching bei München, Germany
[8] Dipartimento di Fisica e Astronomia, Università di Firenze, via G. Sansone 1, I-50019 Sesto Fiorentino, Firenze, Italy
[9] INAF—Osservatorio Astrofisico di Arcetri, Largo Enrico Fermi 5, I-50125 Firenze, Italy

Abstract

We present deep Chandra observations of PSO J231.6576−20.8335, a quasar at redshift $z = 6.59$ with a nearby (∼8 proper kpc) companion galaxy. The Atacama Large Millimeter/submillimeter Array observed both the quasar and companion to be bright in [C II], and the system has significant extended Lyα emission around the quasar, suggesting that a galaxy merger is ongoing. Unlike previous studies of two similar systems, and despite observing the system with Chandra for 140 ks, we do not detect the companion in X-rays. The quasar itself is detected, but only $13.3^{+4.8}_{-3.7}$ net counts are observed. From a basic spectral analysis, the X-ray spectrum of the quasar is soft (hardness ratio of $\mathcal{HR} = -0.60^{+0.17}_{-0.27}$, power-law index of $\Gamma = 2.6^{+1.0}_{-0.9}$), which results in a rest-frame X-ray luminosity comparable to other bright quasars ($L_{2-10} = 1.09^{+2.20}_{-0.70} \times 10^{45}$ erg s^{-1}) despite the faint observed X-ray flux. We highlight two possible interpretations of this result: the quasar has a steep value of Γ—potentially related to observed ongoing Eddington accretion—thereby pushing much of the emission out of our observed band, or the quasar has a more normal spectrum ($\Gamma \sim 2$) but is therefore less X-ray luminous ($L_{2-10} \sim 0.6 \times 10^{45}$ erg s^{-1}).

Unified Astronomy Thesaurus concepts: X-ray quasars (1821); X-ray astronomy (1810); Galaxy mergers (608); Quasars (1319); Quasar-galaxy pairs (1316)

1. Introduction

In the first billion years of the universe ($z \gtrsim 5.7$), supermassive black holes (SMBHs) grew from initial seeds to masses of over $10^9 \, M_\odot$ (e.g., Shen et al. 2019); observed as quasars, the significant early growth of these objects remains an outstanding challenge for cosmology (e.g., Smith & Bromm 2019). Driven by deep infrared surveys and comprehensive spectroscopic follow-up campaigns, the number of quasars known in this redshift regime has risen drastically in the past decade (e.g., Bañados et al. 2014, 2016, 2018b; Venemans et al. 2015; Jiang et al. 2016; Mazzucchelli et al. 2017; Reed et al. 2017, 2019; Matsuoka et al. 2019; Wang et al. 2019b; Yang et al. 2019), providing new opportunities to investigate black hole growth mechanisms. X-ray observations, which offer the best view of the inner accretion region of the active galactic nuclei (AGN) powering quasars (Fabian 2016), are of particular importance for understanding how SMBHs are able to grow so quickly.

While the population of quasars at the highest redshifts has long been speculated to reside in overdense regions (Costa et al. 2014), in recent years a number of works using the Atacama Large Millimeter/submillimeter Array (ALMA) have revealed that a number of these quasars have [C II]-bright companions (Decarli et al. 2017, 2018; Willott et al. 2017; Neeleman et al. 2019; Venemans et al. 2019; see also Farina et al. 2017; D'Odorico et al. 2018). These gas-rich mergers could potentially seed the rapid growth required to explain the early population of SMBHs (Hopkins et al. 2008). In addition, if companion galaxies also host AGN, the resultant SMBH

mergers (Escala et al. 2005), which are invisible to current gravitational-wave observatories (e.g., Salcido et al. 2016), could produce rapid super-Eddington growth; this stochastic growth would, in turn, reduce the need for sustained super-Eddington accretion.

So far, companion galaxies of $z > 6$ quasars are mostly unexplored in X-ray observations, with two exceptions. Vito et al. (2019a) studied PSO J167.6415−13.4960, a $z = 6.52$ quasar with a companion detected in both [C II] and rest-frame UV emission ∼5 pkpc (0″9) away (Willott et al. 2017; Mazzucchelli et al. 2019). In a 59 ks Chandra observation, Vito et al. (2019a) detected three hard energy photons at the location of the system—a significant ($P = 0.9996$) detection implying a heavily obscured quasar, but one which could not be clearly assigned to either the quasar or its companion. Recently, Connor et al. (2019) reported on a 150 ks Chandra observation of PSO J308.0416−21.2339, a $z = 6.23$ quasar with a [C II]- and UV-bright companion visible on both sides of the quasar, indicative of an ongoing merger (Decarli et al. 2017, 2019). Connor et al. (2019) detected three hard energy photons at the brightest knot of UV emission indicative of a dual AGN, but, due to the longer exposure time, the detection was less significant ($P = 0.979$). With no other deep X-ray observations of high-redshift quasar companions reported, further observations are needed to constrain the roles of companions in SMBH growth.

In this work, we focus on and present new deep Chandra observations of PSO J231.6576−20.8335 (hereafter PJ231−20), a $z = 6.5864 \pm 0.0005$ quasar first discovered by Mazzucchelli et al. (2017). PJ231−20's systemic redshift was
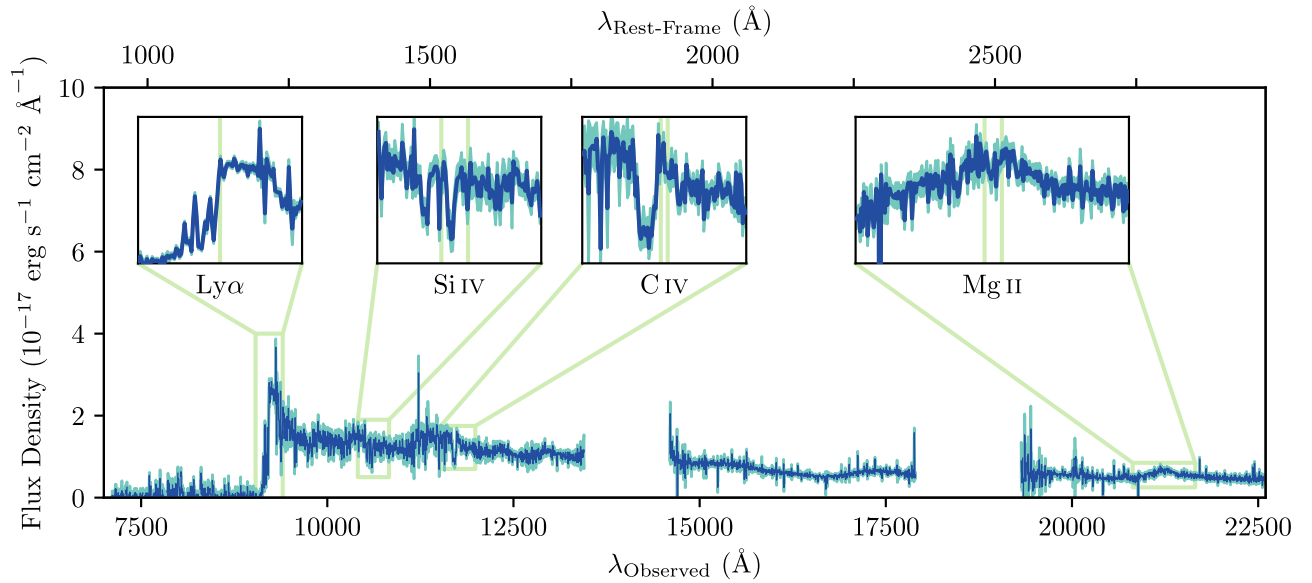
Figure 1. Near-infrared spectrum of PJ231−20 (blue) adapted from Mazzucchelli et al. (2017), with 1σ errors shown in teal. Per that work, this spectrum is flux calibrated to the J band and corrected for the intrinsic reddening of the Milky Way. Four spectral transitions of note are detailed in cutouts, with the wavelength of the associated lines at the adopted redshift of the quasar indicated by the vertical green lines. The spectrum shows high-velocity troughs blueshifted from the high-excitation lines (Si IV and C IV), and we therefore classify PJ231−20 as a HiBAL.

measured by Decarli et al. (2018) from [C II] emission observed with ALMA. In those same ALMA observations, a companion galaxy was detected 8.4 ± 0.6 pkpc ($\sim 1{\farcs}5$) away at a relative velocity of 137 km s^{-1} ($z = 6.5900$; Decarli et al. 2017). Deeper and higher-resolution ALMA observations presented by Neeleman et al. (2019) distinctly resolved both objects,[10] showing compact cores and fainter, extended emission; Neeleman et al. (2019) argue that this extended structure is the result of gas being stripped in the early stages of a merger. Additional extended emission is seen in a rest-frame Lyα halo stretching north of the quasar, as reported by Drake et al. (2019) and Farina et al. (2019). From IR and [C II] measurements, the companion is rapidly forming stars (SFR ~ 750 M$_\odot$ yr^{-1}), yet it has an unobscured star formation rate of SFR$_{\rm UV} < 3$ M$_\odot$ yr^{-1}, implying that the companion is heavily obscured (Mazzucchelli et al. 2019).

The rest-frame UV spectrum of PJ231−20 originally presented by Mazzucchelli et al. (2017) is shown in Figure 1. While the spectrum was analyzed in that work, the quasar itself was not classified. As broad absorption troughs are clearly present slightly blueshifted from the peaks of the Si IV and C IV lines, we classify PJ231−20 as a broad absorption line (BAL) quasar. In particular, this quasar is a high-ionization BAL (HiBAL) quasar (Becker et al. 2000). Based on the UV spectrum, Mazzucchelli et al. (2017) report a black hole of $M_{\rm BH} = 3.05^{+0.44}_{-2.24} \times 10^9$ M$_\odot$ that is accreting at an Eddington ratio of $L_{\rm bol}/L_{\rm Edd} = 0.48^{+0.11}_{-0.39}$. From ALMA observations, Neeleman et al. (2019) calculate a dynamical mass for the host galaxy of $(2.0–6.2) \times 10^{10}$ M$_\odot$ and $(2.7–8.4) \times 10^{10}$ M$_\odot$ for the companion.

We adopt a Galactic neutral hydrogen column density of $N_{\rm H} = 8.35 \times 10^{20}$ cm^{-2} in the direction of PJ231−20 (Kalberla et al. 2005). While Cooper et al. (2019) report a foreground absorption system at $z = 6.476$, it is of low enough

Table 1
Summary of Chandra Observations

Obs ID	Exposure Time (ks)	Start Time (UTC)	
		(YYYY-mm-dd)	(hh:mm:ss)
20469	16.83	2019 May 27	08:00:46
22231	29.67	2019 May 31	01:44:11
22232	21.78	2019 May 31	19:42:49
22233	39.67	2019 Jun 1	14:36:29
22165	32.57	2019 Jun 20	05:36:12

density ($\log[N_{\rm C\,II}/{\rm cm}^{-2}] = 13.5$) that we do not consider its impact on our observations in this work. We use a flat ΛCDM cosmology with $H_0 = 70$ km s^{-1} Mpc^{-1}, $\Omega_M = 0.3$, and $\Omega_\Lambda = 0.7$, and adopt a quasar redshift of $z = 6.5864$, at which the scale is 5.42 pkpc arcsec^{-1}. Errors are reported at the 1σ (68%) confidence level unless otherwise stated. Upper limits correspond to 3σ limits.

2. Observations

We observed PJ231−20 with the Chandra X-ray Observatory for 140.52 ks across five separate visits. The details of these observations are given in Table 1. All observations were conducted with the Advanced CCD Imaging Spectrometer (ACIS; Garmire et al. 2003), with PJ231−20 positioned to be observed with the back-illuminated ACIS S-3 chip. We used the Very Faint telemetry format and the Timed Exposure mode for our observations.

Observations were reduced and analyzed with the Chandra Interactive Analysis of Observations software package (CIAO; Fruscione et al. 2006) v4.11 using CALDB version 4.8.4.1. We first reduced our observations with the `chandra_repro` script, using standard grade, status, and good time filters, as well as accounting for the telemetry format by setting `check_vf_pha=yes`. To minimize the impact of pointing uncertainties from the five observations, we used WAVDETECT (Freeman et al. 2002) and the CIAO tools `wcs_align` and

---

[10] Neeleman et al. (2019) also report a second companion, but as it is an order of magnitude fainter than the first-reported companion in this system, we do not consider it in this work.
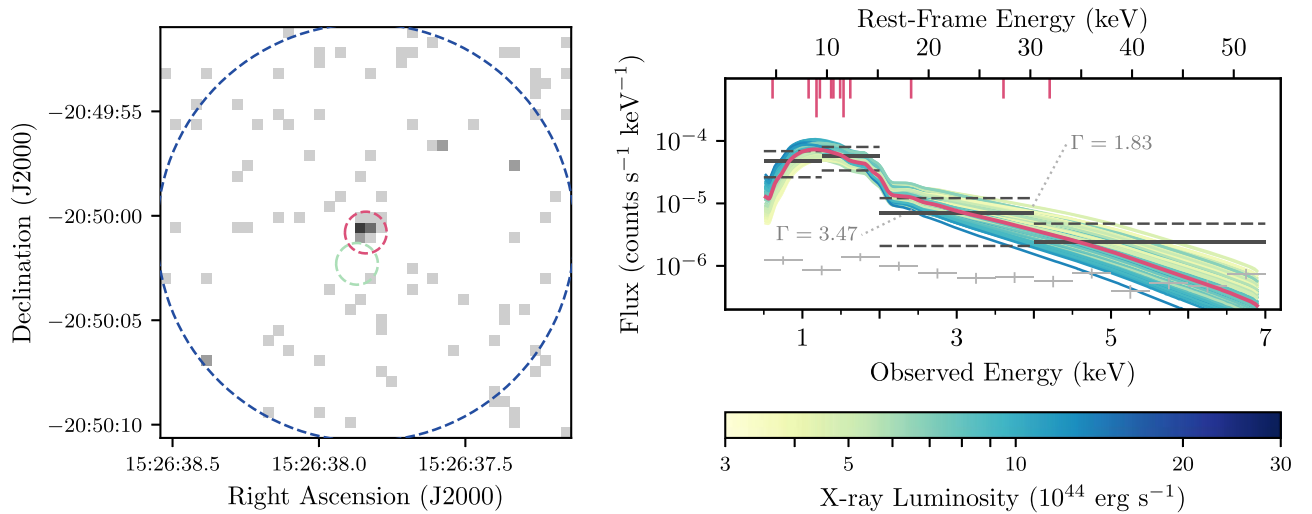
Figure 2. Left: 0.5–7.0 keV Chandra observation of PJ231−20. The quasar and companion are indicated by the red and green circles, respectively, while the large dashed blue circle traces the inner radius of the background annulus. While the quasar is clearly detected, the companion is not. Right: X-ray spectrum of PJ231−20. Data (dark gray) are binned for ease of display, but were not binned during fitting. The best-fitting spectrum is shown in red, while 100 spectra with $\Delta C \leqslant 2.30$ from our Monte Carlo analysis are shown colored by their X-ray luminosity. Higher values of luminosity are derived for softer power-law slopes; Γ values for the two spectra at the extremes are marked. Energies of individual photons detected are indicated by vertical bars at the top of the figure, and the background flux level is shown in light gray in 0.5 keV wide bins.

wcs_update to align all five observations. For imaging analysis, the observations were then combined with the merge_obs script into broad (0.5–7.0 keV), soft (0.5–2.0 keV), and hard (2.0–7.0 keV) images. We then ran the alignment procedure once more, this time using the full depth of our Chandra images to align with the Guide Star Catalog v2.3 (GSC; Lasker et al. 2008). After correction, the absolute astrometry of our observations agreed with that of the GSC to an average of ∼0″.7, and the centroid position of PJ231−20 agrees with the ALMA measurement (Decarli et al. 2017) to less than a pixel (0″.49).

For both photometry and spectroscopy, we used a 1″.0 radius aperture centered on the coordinates of PJ231−20, with a background in a concentric annular region with inner and outer radii of 10″.0 and 30″.0, respectively. A 1″.0 radius aperture was also used to evaluate the companion. Both apertures and the inner radius of the background annulus are shown in Figure 2. We extracted spectra from each individual observation using the task spec_extract with the flag correctpsf=yes. Spectra were combined with the combine_spectra task and analyzed with XSPEC v12.10.1 (Arnaud 1996) through the Python-based PyXspec.

3. X-Ray Properties of PJ231−20

In the broad band, we detect PJ231−20 with $13.3^{+4.8}_{-3.7}$ net counts, computing source statistics with the method of Gehrels (1986). In the same photometric aperture, we detect $10.8^{+4.4}_{-3.3}$ and $2.5^{+2.9}_{-1.7}$ net counts in the soft and hard bands, respectively, up to a maximum detected energy of 4.20 keV. The hard band detection on its own would only be expected as a background fluctuation with probability $P = 0.0118$, using binomial statistics (Weisskopf et al. 2007). From these photons, we compute the hardness ratio, $\mathcal{HR}$,[11] using the Bayesian methodology described by Park et al. (2006). Assuming uniform (Jeffreys) priors and integrating the posterior

distribution with Gaussian quadrature, we find $\mathcal{HR} = -0.60^{+0.17}_{-0.27}$. In comparison, for PSO J308.0416 −21.2339, another $z > 6$ quasar with a [C II]-bright companion, Connor et al. (2019) report an observed $\mathcal{HR} = -0.48^{+0.11}_{-0.10}$ with a best-fit power-law index of $\Gamma = 2.39^{+0.37}_{-0.36}$.

To place further constraints on the properties of the quasar, we fit the X-ray spectrum in XSPEC. With so few counts, we do not bin the spectrum, and we use the modified C-Statistic (C, Cash 1979; Wachter et al. 1979) to find the parameters of the best fit. As both the source and the background are Poisson data, the spectral fitting does not subtract a background, but instead accounts for both the model and the background simultaneously when evaluating the quasar spectrum (XSPEC's W Statistic). We adopt the simple spectral model of phabs × powerlaw, with N_H frozen at its adopted value. The only parameters allowed to vary are the normalization of the power law and the spectral slope, Γ, so that 1σ uncertainties include all values where $\Delta C \leqslant 2.30$ (e.g., Lampton et al. 1976; as noted by Cash 1979, ΔC behaves as $\Delta\chi^2$ for evaluating confidence intervals).

We find the best fit for our spectrum with $\Gamma = 2.6^{+1.0}_{-0.9}$, and a corresponding broadband flux of $F_{0.5-7.0} = 1.5^{+0.8}_{-0.5} \times 10^{-15}$ erg s^{-1} cm^{-2} and an unobscured luminosity in the rest-frame 2.0–10.0 keV band of $L_{2-10} = 1.09^{+2.20}_{-0.70} \times 10^{45}$ erg s^{-1}, where the uncertainties in flux and luminosity include those of both fitted parameters. The results of our fit are summarized in Table 2. The observed data, as well as 100 spectra from a Monte Carlo exploration of the parameter space, are shown in the right panel of Figure 2. The Markov Chain Monte Carlo method used to generate these spectra was the XSPEC routine chain using the Goodman & Weare (2010) algorithm, with a burn length of 500 steps and a run length of 2500 steps. As shown in Figure 2, the measured luminosity is being driven to higher values by an extrapolation of an extremely soft power-law index (see Vito et al. 2019b) into the rest-frame soft-energy bands. If we fix Γ to $\Gamma = 2.2$ (as found by Vito et al. 2019b to be representative of $z > 6$

---
[11] $\mathcal{HR} = (H - S)/(H + S)$, where H and S are the net counts in the hard (2.0–7.0 keV) and soft (0.5–2.0 keV) bands, respectively.

Table 2
X-Ray Properties

Parameter	Value	Units
Net Counts	$13.3^{+4.8}_{-3.7}$	⋯
Soft Counts	$10.8^{+4.4}_{-3.3}$	⋯
Hard Counts	$2.5^{+2.9}_{-1.7}$	⋯
$\mathcal{HR}$	$-0.60^{+0.17}_{-0.27}$	⋯
Γ	$2.6^{+1.0}_{-0.9}$	⋯
L_{2-10}	$1.09^{+2.20}_{-0.70} \times 10^{45}$	erg s^{-1}
$F_{0.5-2.0}$	$1.0^{+0.8}_{-0.4} \times 10^{-15}$	erg s^{-1} cm^{-2}
$F_{0.5-7.0}$	$1.5^{+0.8}_{-0.5} \times 10^{-15}$	erg s^{-1} cm^{-2}
$\alpha_{\rm OX}$	$-1.63^{+0.30}_{-0.27}$	⋯
C/d.o.f	78.7 / 444	⋯

quasars) or $\Gamma = 1.9$ (typical of the quasar population in general; e.g., Nanni et al. 2017), we find best-fit luminosities of $L_{2-10} = 0.70 \times 10^{45}$ erg s^{-1} and $L_{2-10} = 0.51 \times 10^{45}$ erg s^{-1}, respectively.

Other analyses of high-redshift quasars (Ai et al. 2017; Nanni et al. 2018; Connor et al. 2019) have also included the contributions from obscuration at the redshift of the quasar in their spectral fitting. With only 14 observed counts, adding a third free component to our model is ill advised (and impractical). However, if we fix $\Gamma = 2.6$ and model the spectrum with the XSPEC model zphabs × phabs × powerlaw, again fixing the redshift and Galactic column density to their adopted values, we find that the 1σ uncertainties on the redshifted column density are $N_{H,z} \in [0.00, 4.8] \times 10^{23}$ cm^{-2}. With such large uncertainties, we do not gain any meaningful insight by including this term; and, as Chandra is insensitive to obscurations of $\lesssim 10^{23}$ cm^{-2} at these redshifts, ignoring zphabs does not affect our fitted results. We therefore do not include the zphabs term in the remainder of our analysis, although we do discuss the potential of large obscuration in Section 5.

Finally, we estimate the X-ray-to-optical power-law slope, and compare the measured X-ray luminosity to that predicted from the brightness reported by Mazzucchelli et al. (2017). We characterize the X-ray-to-optical power-law slope with $\alpha_{\rm OX}$, defined as

$$\alpha_{\rm OX} = 0.3838 \times \log(L_{2\,\rm keV}/L_{2500\,\text{Å}}), \qquad (1)$$

where $L_{2\,\rm keV}$ and $L_{2500\,\text{Å}}$ are the monochromatic luminosities at rest-frame 2 keV and 2500 Å, respectively. Mazzucchelli et al. (2017) report a flux density of $F_{2500\,\text{Å}} = 5.04^{+0.03}_{-0.75} \times 10^{-18}$ erg s^{-1} cm^{-2} Å^{-1} as measured from the NIR spectrum. Accounting for redshift k-corrections, this translates to a value of $L_{2500\,\text{Å}} = 3.95 \times 10^{31}$ erg s^{-1} Hz^{-1}. From our data, we find $\alpha_{\rm OX} = -1.63^{+0.30}_{-0.27}$. For comparison, from the calculated value of $L_{2500\,\text{Å}}$ and from the observed relation of Lusso & Risaliti (2016), we would expect $\alpha_{\rm OX} = -1.74^{+0.23}_{-0.23}$ (both sets of $\alpha_{\rm OX}$ errors include the uncertainties on $L_{2500\,\text{Å}}$). The observed value of $\alpha_{\rm OX}$ is shown relative to that of low-redshift and other high-redshift quasars, as well as the fitted relation from Lusso & Risaliti (2016), in Figure 3.

As a final note on our spectral fitting, we consider the effects of fitted bandpass and background region. All of our analyses were conducted in the traditional broad band (0.5–7.0 keV); however, as shown in Figure 2, most of the observed flux is at soft energies. To see if including noisier energy ranges affected our results, we again fit the data, this time limiting ourselves to only 0.5–3.0 keV. However, we find that the results are not significantly changed, with a best-fit value of $\Gamma = 2.7^{+1.2}_{-1.3}$. We also tested the effect of varying the size of the region used for background extraction; systematic uncertainties produced by this selection are of order one-tenth the statistical uncertainties in our fit.

4. Companion

PJ231−20 was targeted for observations with Chandra in part to search for X-ray emission from the companion detected by Decarli et al. (2017). However, unlike PSO J308.0416 −21.2339 (Connor et al. 2019), where both the quasar and companion were seen, the companion here is not even detected at low significance. No photons are detected within $0\rlap{.}''9$ of the companion's position, and only one photon is observed within $1\rlap{.}''0$. This photon has energy 846 eV; the encircled energy fraction for Chandra sources at this energy exceeds 80% within $0\rlap{.}''5$. In contrast, the probability of one photon arising in this aperture based on the measured background in the broad band is $P = 0.51$, based on binomial statistics (Weisskopf et al. 2007; Lansbury et al. 2014). As the probability of being a background fluctuation exceeds that of being a companion photon, we assume that we have detected no net flux from the companion itself. Here, we discuss what this nondetection means for both this companion and other [C II]-detected companions in general.

First, we evaluate limits on the potential luminosity of the companion. Assuming Poisson statistics, the probability of zero photons being detected reaches $P = 0.00135$ (i.e., a 3σ event) when the expected value is 6.61 photons. Using the XSPEC model zphabs × phabs × powerlaw and the response files of our observation, we calculate the unobscured luminosity of a model with 6.61 predicted counts. For a redshifted absorber of column density $N_{H,z} = 10^{23}$ cm^{-2}, the limiting luminosity is 3.0×10^{44} erg s^{-1} ($\Gamma = 2.0$) or 5.9×10^{44} erg s^{-1} ($\Gamma = 2.6$). For a Compton-thick source ($N_{H,z} = \sigma_{\rm T}^{-1} = 1.5 \times 10^{24}$ cm^{-2}), these luminosities become 6.3×10^{44} erg s^{-1} ($\Gamma = 2.0$) and 15.2×10^{44} erg s^{-1} ($\Gamma = 2.6$). Barring extreme levels of obscuration, we can therefore rule out an AGN in the companion with luminosity similar to that of the optically selected quasar, despite both galaxies having similar masses.

A lack of observed emission from the companion is perhaps not surprising when considering the earlier work of Mazzucchelli et al. (2019). They reported that the companion is also not detected in rest-frame UV or optical emission, implying a significant amount of dust obscuration. Indeed, the spectral energy distribution of the companion as presented in that work is most like Arp 220, a well-known ultraluminous infrared galaxy in the local universe, being both highly star forming and highly dust obscured. The X-ray luminosity of the AGN in Arp 220 is of order $L_{2-10} \lesssim 10^{42}$ erg s^{-1} (Paggi et al. 2017), and no AGN emission is seen in hard X-rays by the Nuclear Spectroscopic Telescope Array (NuSTAR; Teng et al. 2015). As Arp 220 has an SMBH with mass of order $\sim 10^9 \, M_\odot$ (Scoville et al. 2017), and as the $\sim 100 \, \mu$m rest-frame luminosities of Arp 220 and the companion only differ by a factor of ~ 1.4 (Mazzucchelli et al. 2019), it is thus possible to envision that the companion might only host a faint AGN.
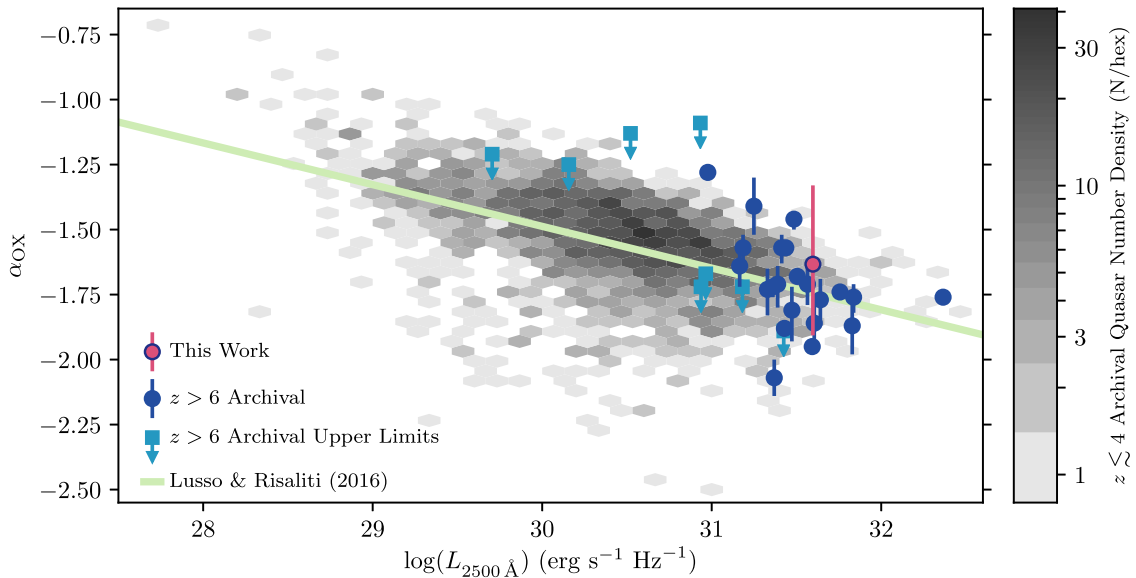
Figure 3. Distribution of α_{OX} as a function of rest-frame 2500 Å luminosity for high-redshift ($z > 6$; points) and low-redshift ($z \lesssim 4$, grayscale density plot) quasars, with PJ231−20 highlighted. The underlying distribution and the best fit to this trend (indicated by the green line) are both from Lusso & Risaliti (2016), which is based on spectroscopically confirmed broad-line quasars with XMM observations. The high-redshift population is drawn from the compilation of Vito et al. (2019b), with later additions from Connor et al. (2019) and Pons et al. (2020).

Looking toward the broader population of [C II]-detected companions (six such systems are known at $z \gtrsim 6$; Decarli et al. 2017; Willott et al. 2017; Neeleman et al. 2019), the nondetection in X-rays of a companion around PJ231−20 represents the first complete nondetection in three such systems well studied so far (Vito et al. 2019a; Connor et al. 2019). We note that SDSS J0842+1218 has also been observed in X-rays (Vito et al. 2019b) and that no emission from its companion was seen; however, these observations were relatively short (29 ks), and so we treat the companion as being unobserved in this discussion. The two potentially detected companions (PSO J308–21 and PSO J167–13) are in systems far along in the merging process (with projected separations of $\lesssim 10$ pkpc), as is one of the unobserved companion systems (SDSS J1306 +0356). However, the other two remaining systems (SDSS J0842+1218 and CFHQ J2100–1715) are more like PJ231 −20, with spectral energy distributions being dominated by star formation and dust obscuration (Mazzucchelli et al. 2019) and with star-forming companions that are still tens of kiloparsecs away from merging. Circosta et al. (2019) recently put forward a model that, in the early universe, the dense interstellar medium of galaxies can cause obscuration supplementing or even surpassing that of the circumnuclear gas; in this context, AGN in companions might only be visible once a merger has begun to disrupt the gas distribution in the companion galaxy. It seems likely, therefore, that while a quasar may have a [C II]-bright companion, that should not be taken as an indication of an X-ray-visible AGN in the companion, at least with current facilities.

5. Interpretations

With so few counts detected in the X-ray spectrum of PJ231 −20 despite the long exposure (see Bañados et al. 2018a), it is difficult to definitively establish the properties of the AGN powering the quasar emission. Here, we discuss two possible interpretations to explain the data. First, we consider if the quasar spectrum is indeed as soft in the X-rays as given by the

best fit, such that it still has an X-ray luminosity of the order 10^{45} erg s^{-1} despite its faint observed flux. Alternatively, we consider if the quasar spectrum is typical ($\Gamma \approx 2.0$), in which case there is not significant flux just below our soft-energy cutoff, and the quasar is thus not highly luminous in X-rays. Finally, we discuss what effects obscuration and variability could have on our interpretations.

5.1. Soft X-Ray Spectrum

The first interpretation of these results is that the best fit is accurate—the X-ray spectrum of PJ231−20 is very soft, driving a fairly normal X-ray luminosity despite the small number of observed photons. In this context, the low count rate is a product of Chandra sampling far down the quasar's power-law spectrum due to the high redshift (a schematic of this interpretation is given in Figure 4). If this interpretation holds, and if PJ231−20 is representative of some population of high-redshift quasars, it spells trouble for deeper studies with currently available facilities.

One potential reason for this spectral shape is that PJ231−20 is undergoing a significant burst of accretion in connection with the ongoing merger. A number of works (e.g., Pounds et al. 1995; Bian & Zhao 2003; Porquet et al. 2004; Brightman et al. 2013, 2016; Trakhtenbrot et al. 2017; Ricci et al. 2018; Wang et al. 2019a) have identified a trend between Γ and λ_{Edd}, where $\lambda_{Edd} = L_{bol}/L_{Edd}$, such that larger values of Γ trend with increasing Eddington ratios. PJ231−20 is accreting at an Eddington ratio of $\lambda_{Edd} = 0.48^{+0.11}_{-0.39}$ (Mazzucchelli et al. 2017), although we note that the black hole mass—and thus the Eddington ratio—were derived using a relation with a 0.55 dex scatter on its zero-point (Vestergaard & Peterson 2006), and thus Eddington or even super-Eddington accretion is not incompatible with previous data. For reference, the best-fit Γ predicted by the relation of Brightman et al. (2016) for $\lambda_{Edd} = 0.48$ is $\Gamma = 2.25$, although due to the significant uncertainties in both λ_{Edd} and the scaling relation, this value is suggestive, not predictive.
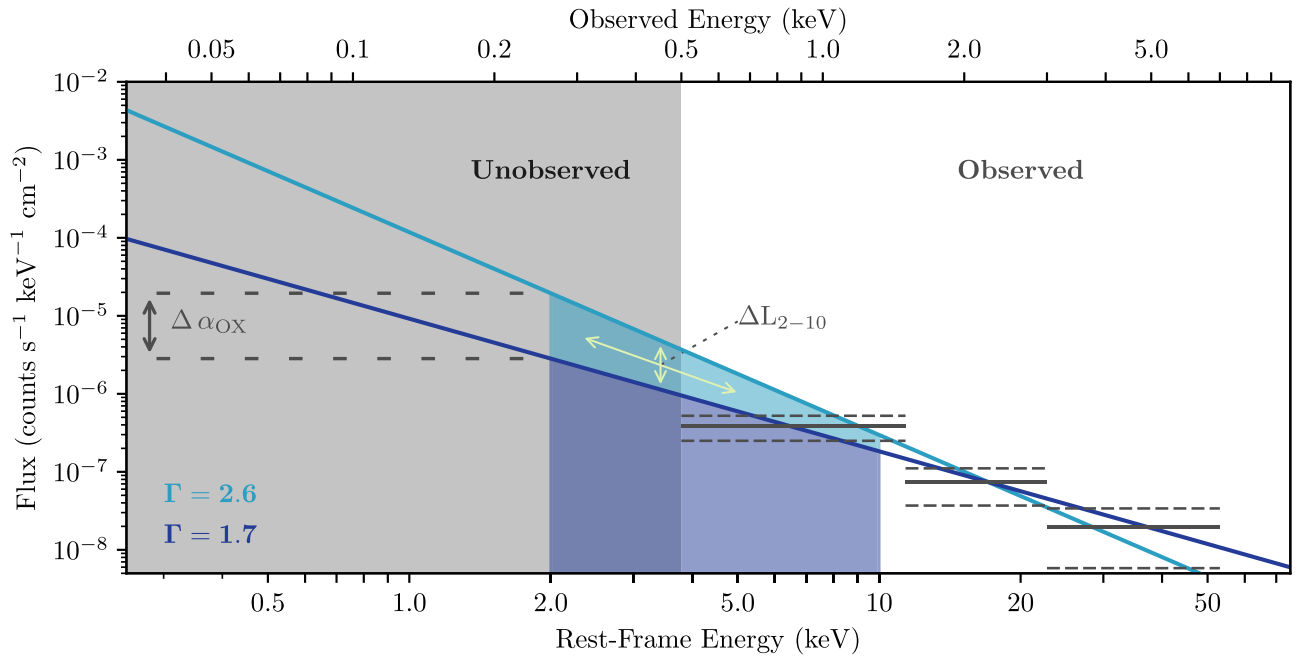
Figure 4. Conceptual model of how interpreting PJ231−20 as either soft (light blue) or faint (dark blue) affect calculated properties of the quasar. Our observed data (here corrected for the differing response of Chandra with energy) are shown binned by horizontal bars, with 1σ uncertainties as dashed lines above and below. The energy domain where we lack observations is indicated by the shaded gray region. Two power-law spectra—which are toy models, not fits—are shown; it is clear from this demonstration that both α_{OX} and L_{2-10} are driven by extrapolations into the regime where we lack observations.

Previous works have explained this correlation between Γ and λ_{Edd} by arguing that an enhancement in accretion will lead to a stronger UV flux from the accretion disk, which in turn more effectively cools the electron corona (e.g., Brightman et al. 2013). A cooler corona, in turn, produces a softer photon index, all other things being equal (e.g., Ricci et al. 2018). While it may be tempting to consider the large Lyα halo around PJ231−20 reported by Drake et al. (2019) and Farina et al. (2019) as a source of excess UV photons, the low luminosity ($L_{Ly\alpha} \sim 10^{44}$ erg s^{-1}) and large spatial extent of the halo itself ($\sim$6.6 arcsec^2) make its UV contribution to the corona negligible.

Our best-fit spectrum has $\Gamma = 2.6^{+1.0}_{-0.9}$, which is softer than expected of low-redshift AGN (albeit within 1σ); in a fit of $\sim$800 bright, $z \lesssim 0.4$ AGN, Ricci et al. (2017) report a median $\Gamma \approx 1.8$, with 90% of the values falling between $1.3 \lesssim \Gamma \lesssim 2.2$. However, the observed value of Γ for PJ231−20 is not particularly extreme for high-redshift quasars. In their analysis of $z > 6$ AGN, Vito et al. (2019b) report an average value of $\langle\Gamma\rangle = 2.20^{+0.39}_{-0.34}$ for sources with fewer than 30 detected counts and an average $\langle\Gamma\rangle = 2.13^{+0.13}_{-0.13}$ for quasars with at least 30 counts. The only other clearly detected high-redshift quasar with a [C II]-bright companion, PSO J308.0416 −21.2339, also has a high power-law index: $\Gamma = 2.39^{+0.37}_{-0.36}$ (Connor et al. 2019). Nanni et al. (2018) describe a change in Γ for one particular $z \sim 6.3$ quasar over a 13 yr baseline, where early observations are best fit by $\Gamma = 2.37^{+0.16}_{-0.15}$ in a 2003 XMM observation and $\Gamma = 1.81^{+0.18}_{-0.18}$ in a 2017 Chandra observation (we discuss the potential of variability below). From this, it seems as if PJ231−20 having an intrinsically soft value of Γ is plausible.

5.2. Typical X-Ray Spectrum

A second interpretation of the data is that PJ231−20 is not a highly luminous AGN ($L_{2-10} < 10^{45}$ erg s^{-1}; e.g., Georgakakis et al. 2015; Khorunzhev et al. 2018), and that the small number of detected counts is indicative of a quasar producing relatively few X-ray photons, both in and out of the observed X-ray bands (see Figure 4). In this context, Γ is most likely toward the lower end of the 1σ distribution of our best-fit values, but is, in turn, less of an outlier from the overall distribution of AGN properties. Even for shallow power-law slopes, small number statistics and Chandra's soft-energy response combine for a spectrum dominated by soft photons when only few counts are present; this is true without needing to invoke an extreme value of Γ. Through that lens, our X-ray data are still in keeping with a harder, fainter source.

As discussed in Section 3, a lower value of Γ reduces the luminosity of PJ231−20 to $L_{2-10} \lesssim 0.7 \times 10^{45}$ erg s^{-1}. This luminosity is either around or slightly fainter than the knee of the AGN luminosity function for $z \gtrsim 4$, which various works have measured to be $L^*_{2-10} \approx (0.5-1.0) \times 10^{45}$ erg s^{-1} (Vito et al. 2014; Georgakakis et al. 2015; Khorunzhev et al. 2018). Likewise, with an absolute magnitude of $M_{1450} = -27.14$, PJ231−20 does not have an extreme UV luminosity (Manti et al. 2017; Kulkarni et al. 2019). As an otherwise normal quasar, the simple explanation for PJ231−20 is that its true value of Γ is closer to that of a typical quasar, which, even for higher redshifts, is shallower than that found by the best fit.

We also note that, as shown in Figure 1 and discussed in Section 1, the NIR spectrum of PJ231−20 shows evidence of being a BAL quasar. BALs are routinely observed to be X-ray faint for their rest-frame UV luminosity (e.g., Gibson et al. 2009), as characterized by $\Delta\alpha_{OX} = \alpha_{OX,Observed} - \alpha_{OX,Model}$, the difference between observed and predicted values of α_{OX}. While obscuration could be invoked for this correlation, studies with NuSTAR (e.g., Luo et al. 2014) and with moderate-

redshift AGN (e.g., Morabito et al. 2014) have shown that BAL spectra, when accounting for obscuration, still have extrapolated values of α_{OX} lower than predicted by their $L_{2500\,\text{Å}}$. Of course, even for the lowest value of α_{OX} allowed by the 1σ uncertainties, PJ231−20 is still within the scatter of the Lusso & Risaliti (2016) fit. In addition, the trend of large, negative values of $\Delta\alpha_{OX}$ with BALs is reduced for BALs with absorption lines of relatively low depth such as PJ231−20 (Vito et al. 2018). Nevertheless, a lower value of α_{OX} as would be caused by a typical value of Γ is more in keeping with the rest-frame UV spectrum.

5.3. Other Concerns

One potential explanation for an observed X-ray faintness is heavy dust obscuration of the AGN, but this does not mesh with the observed data. The observed hardness ratio of PJ231 −20, $\mathcal{HR} = -0.60^{+0.17}_{-0.27}$ (see also Figure 2), implies that most of the observed flux is at relatively soft energies. If a significant screen of dust existed, we would expect it to drive the hardness ratio to much harder values. Likewise, the broad Mg II emission (FWHM $\sim$ 4700 km s^{-1}) reported by Mazzucchelli et al. (2017; see also Figure 1) indicates that PJ231−20 is a Type 1 AGN; Type 1 AGN have long been seen to have minimal amounts of dust ($N_H \lesssim 10^{22}$ cm^{-2}; e.g., Shimizu et al. 2018). Due to the extreme redshift of PJ231−20, such column densities would have no impact on our observed spectrum. Thus, we do not expect dust to be responsible for the observed faintness of PJ231−20.

Previous optical and near-infrared observations of the PJ231 −20 system, as reported by Mazzucchelli et al. (2017, 2019), Drake et al. (2019), and Farina et al. (2019), were conducted between 2015 March and 2017 July. The X-ray observations described here, however, took place almost 2 yr afterward (see Table 1). It is therefore possible that the physical conditions of the AGN changed during that time—although we note that a temporal offset of Δt in the observed frame corresponds to an offset of $\Delta t/(1 + z)$ in the rest frame of the AGN. Previously, Page et al. (2014) reported an X-ray luminosity drop of $\sim$2× over 15 months (observed) for a $z \sim 7.1$ quasar, and Nanni et al. (2018) report variability over observed timescales of 16 months (low significance) and 14 yr for one $z = 6.31$ quasar, where total fluctuations were again on the order of 2×. It is thus unlikely that the observed X-ray photon faintness was caused by variability alone.

6. Summary

We have presented deep (140 ks) Chandra observations of PJ231−20, a $z = 6.59$ quasar with a nearby (8 pkpc) companion detected in [C II] with ALMA. Our primary results are:

1. PJ231−20 is detected in the X-ray observations, with $13.3^{+4.8}_{-3.7}$ counts. The source is very soft, having a hardness ratio of $\mathcal{HR} = -0.60^{+0.17}_{-0.27}$. While the small number of detected counts makes the results of spectral fitting uncertain, a simple power-law model best fits the data with $\Gamma = 2.6^{+1.0}_{-0.9}$.
2. Despite the faint detection, the rest-frame 2.0–10.0 keV luminosity is reasonable for the SMBH mass powering the PJ231−20 quasar: $L_{2-10} = 1.09^{+2.20}_{-0.70} \times 10^{45}$ erg s^{-1}. However, the luminosity is heightened by the large value of Γ; if Γ is fixed to 2.2, more typical of high-redshift

quasars, the best-fit luminosity drops to $L_{2-10} = 0.70 \times 10^{45}$ erg s^{-1}.
3. The companion galaxy is not detected in X-rays. While at least one other companion galaxy has been detected by Chandra around a different $z > 6$ quasar (Connor et al. 2019), previous Hubble Space Telescope observations revealed that the companion to PJ231−20 is heavily obscured (Mazzucchelli et al. 2019). If an AGN is present, it is too faint and/or obscured to be visible to current X-ray facilities.
4. We discussed two potential interpretations of the observed properties of PJ231−20. First, that it has an extremely soft power-law index, and therefore most of the emission is below that observable by Chandra. Second, that Γ is actually smaller, and that the quasar is not highly luminous in the rest-frame soft X-ray band. Neither variability nor obscuration by themselves appear to play a significant role in explaining the small number of observed photons.

To better understand the conditions of the AGN of PJ231 −20, further observations are required—specifically, deeper X-ray observations. XMM-Newton, which has a larger effective area than Chandra that extends to softer energies (0.2 keV), may even allow for a characterization of PJ231 −20's AGN with only a modest exposure time. However, current facilities are being pushed to their limits to observe high-redshift quasars, and deeper understanding will only come with the launch of Athena (Nandra et al. 2013) and, hopefully, Lynx (Gaskin et al. 2019) and AXIS (Mushotzky et al. 2019).

ORCID iDs

Thomas Connor ⬤ https://orcid.org/0000-0002-7898-7664
Eduardo Bañados ⬤ https://orcid.org/0000-0002-2931-7824
Chiara Mazzucchelli ⬤ https://orcid.org/0000-0002-5941-5214
Daniel Stern ⬤ https://orcid.org/0000-0003-2686-9241
Roberto Decarli ⬤ https://orcid.org/0000-0002-2662-8803
Xiaohui Fan ⬤ https://orcid.org/0000-0003-3310-0131
Emanuele Paolo Farina ⬤ https://orcid.org/0000-0002-6822-2254
Elisabeta Lusso ⬤ https://orcid.org/0000-0003-0083-1157

Marcel Neeleman ● https://orcid.org/0000-0002-9838-8191
Fabian Walter ● https://orcid.org/0000-0003-4793-7880

References

Ai, Y., Fabian, A. C., Fan, X., et al. 2017, MNRAS, 470, 1587
Arnaud, K. A. 1996, in ASP Conf. Ser. 101, Astronomical Data Analysis Software and Systems V, ed. G. H. Jacoby & J. Barnes (San Francisco, CA: ASP), 17
Bañados, E., Connor, T., Stern, D., et al. 2018a, ApJL, 856, L25
Bañados, E., Venemans, B. P., Decarli, R., et al. 2016, ApJS, 227, 11
Bañados, E., Venemans, B. P., Mazzucchelli, C., et al. 2018b, Natur, 553, 473
Bañados, E., Venemans, B. P., Morganson, E., et al. 2014, AJ, 148, 14
Barrett, P. E., & Bridgman, W. T. 1999, in ASP Conf. Ser. 172, Astronomical Data Analysis Software and Systems VIII, ed. D. M. Mehringer, R. L. Plante, & D. A. Roberts (San Francisco, CA: ASP), 483
Becker, R. H., White, R. L., Gregg, M. D., et al. 2000, ApJ, 538, 72
Bian, W., & Zhao, Y. 2003, MNRAS, 343, 164
Brightman, M., Masini, A., Ballantyne, D. R., et al. 2016, ApJ, 826, 93
Brightman, M., Silverman, J. D., Mainieri, V., et al. 2013, MNRAS, 433, 2485
Cash, W. 1979, ApJ, 228, 939
Circosta, C., Vignali, C., Gilli, R., et al. 2019, A&A, 623, A172
Connor, T., Bañados, E., Stern, D., et al. 2019, ApJ, 887, 171
Cooper, T. J., Simcoe, R. A., Cooksey, K. L., et al. 2019, ApJ, 882, 77
Costa, T., Sijacki, D., Trenti, M., & Haehnelt, M. G. 2014, MNRAS, 439, 2146
Decarli, R., Dotti, M., Bañados, E., et al. 2019, ApJ, 880, 157
Decarli, R., Walter, F., Venemans, B. P., et al. 2017, Natur, 545, 457
Decarli, R., Walter, F., Venemans, B. P., et al. 2018, ApJ, 854, 97
D'Odorico, V., Feruglio, C., Ferrara, A., et al. 2018, ApJL, 863, L29
Drake, A. B., Farina, E. P., Neeleman, M., et al. 2019, ApJ, 881, 131
Escala, A., Larson, R. B., Coppi, P. S., & Mardones, D. 2005, ApJ, 630, 152
Fabian, A. C. 2016, AN, 337, 375
Farina, E. P., Arrigoni-Battaia, F., Costa, T., et al. 2019, ApJ, 887, 196
Farina, E. P., Venemans, B. P., Decarli, R., et al. 2017, ApJ, 848, 78
Freeman, P. E., Kashyap, V., Rosner, R., & Lamb, D. Q. 2002, ApJS, 138, 185
Fruscione, A., McDowell, J. C., Allen, G. E., et al. 2006, Proc. SPIE, 6270, 62701V
Garmire, G. P., Bautz, M. W., Ford, P. G., Nousek, J. A., & Ricker, G. R. J. 2003, Proc. SPIE, 4851, 28
Gaskin, J. A., Swartz, D. A., Vikhlinin, A., et al. 2019, JATIS, 5, 021001
Gehrels, N. 1986, ApJ, 303, 336
Georgakakis, A., Aird, J., Buchner, J., et al. 2015, MNRAS, 453, 1946
Gibson, R. R., Jiang, L., Brandt, W. N., et al. 2009, ApJ, 692, 758
Goodman, J., & Weare, J. 2010, Commun. Appl. Math. Comput. Sci., 5, 65
Hopkins, P. F., Hernquist, L., Cox, T. J., & Kereš, D. 2008, ApJS, 175, 356
Jiang, L., McGreer, I. D., Fan, X., et al. 2016, ApJ, 833, 222
Kalberla, P. M. W., Burton, W. B., Hartmann, D., et al. 2005, A&A, 440, 775
Khorunzhev, G. A., Sazonov, S. Y., & Burenin, R. A. 2018, AstL, 44, 500
Kulkarni, G., Worseck, G., & Hennawi, J. F. 2019, MNRAS, 488, 1035

Lampton, M., Margon, B., & Bowyer, S. 1976, ApJ, 208, 177
Lansbury, G. B., Alexander, D. M., Del Moro, A., et al. 2014, ApJ, 785, 17
Lasker, B. M., Lattanzi, M. G., McLean, B. J., et al. 2008, AJ, 136, 735
Luo, B., Brandt, W. N., Alexander, D. M., et al. 2014, ApJ, 794, 70
Lusso, E., & Risaliti, G. 2016, ApJ, 819, 154
Manti, S., Gallerani, S., Ferrara, A., Greig, B., & Feruglio, C. 2017, MNRAS, 466, 1160
Matsuoka, Y., Onoue, M., Kashikawa, N., et al. 2019, ApJL, 872, L2
Mazzucchelli, C., Bañados, E., Venemans, B. P., et al. 2017, ApJ, 849, 91
Mazzucchelli, C., Decarli, R., Farina, E. P., et al. 2019, ApJ, 881, 163
Morabito, L. K., Dai, X., Leighly, K. M., Sivakoff, G. R., & Shankar, F. 2014, ApJ, 786, 58
Mushotzky, R., Aird, J., Barger, A. J., et al. 2019, BAAS, 51, 107
Nandra, K., Barret, D., Barcons, X., et al. 2013, arXiv:1306.2307
Nanni, R., Gilli, R., Vignali, C., et al. 2018, A&A, 614, A121
Nanni, R., Vignali, C., Gilli, R., Moretti, A., & Brand t, W. N. 2017, A&A, 603, A128
Neeleman, M., Bañados, E., Walter, F., et al. 2019, ApJ, 882, 10
Page, M. J., Simpson, C., Mortlock, D. J., et al. 2014, MNRAS, 440, L91
Paggi, A., Fabbiano, G., Risaliti, G., et al. 2017, ApJ, 841, 44
Park, T., Kashyap, V. L., Siemiginowska, A., et al. 2006, ApJ, 652, 610
Pons, E., McMahon, R. G., Banerji, M., & Reed, S. L. 2020, MNRAS, 491, 3884
Porquet, D., Reeves, J. N., O'Brien, P., & Brinkmann, W. 2004, A&A, 422, 85
Pounds, K. A., Done, C., & Osborne, J. P. 1995, MNRAS, 277, L5
Reed, S. L., Banerji, M., Becker, G. D., et al. 2019, MNRAS, 487, 1874
Reed, S. L., McMahon, R. G., Martini, P., et al. 2017, MNRAS, 468, 4702
Ricci, C., Ho, L. C., Fabian, A. C., et al. 2018, MNRAS, 480, 1819
Ricci, C., Trakhtenbrot, B., Koss, M. J., et al. 2017, ApJS, 233, 17
Salcido, J., Bower, R. G., Theuns, T., et al. 2016, MNRAS, 463, 870
Scoville, N., Murchikova, L., Walter, F., et al. 2017, ApJ, 836, 66
Shen, Y., Wu, J., Jiang, L., et al. 2019, ApJ, 873, 35
Shimizu, T. T., Davies, R. I., Koss, M., et al. 2018, ApJ, 856, 154
Smith, A., & Bromm, V. 2019, ConPh, 60, 111
Teng, S. H., Rigby, J. R., Stern, D., et al. 2015, ApJ, 814, 56
Trakhtenbrot, B., Ricci, C., Koss, M. J., et al. 2017, MNRAS, 470, 800
Venemans, B. P., Bañados, E., Decarli, R., et al. 2015, ApJL, 801, L11
Venemans, B. P., Neeleman, M., Walter, F., et al. 2019, ApJL, 874, L30
Vestergaard, M., & Peterson, B. M. 2006, ApJ, 641, 689
Vito, F., Brandt, W. N., Bauer, F. E., et al. 2019a, A&A, 628, L6
Vito, F., Brandt, W. N., Bauer, F. E., et al. 2019b, A&A, 630, A118
Vito, F., Brandt, W. N., Luo, B., et al. 2018, MNRAS, 479, 5335
Vito, F., Gilli, R., Vignali, C., et al. 2014, MNRAS, 445, 3557
Wachter, K., Leach, R., & Kellogg, E. 1979, ApJ, 230, 274
Wang, C., Yu, L.-M., Bian, W.-H., & Zhao, B.-X. 2019a, MNRAS, 487, 2463
Wang, F., Yang, J., Fan, X., et al. 2019b, ApJ, 884, 30
Weisskopf, M. C., Wu, K., Trimble, V., et al. 2007, ApJ, 657, 1026
Willott, C. J., Bergeron, J., & Omont, A. 2017, ApJ, 850, 108
Yang, J., Wang, F., Fan, X., et al. 2019, AJ, 157, 236